JOURNAL OF COMPUTATIONAL PHYSICS **130,** 77–91 (1997)
ARTICLE NO. CP965553

Compact High-Order Accurate Nonlinear Schemes

Xiaogang Deng* and Hiroshi Maekawa†

*Computational Aerodynamic Institute, P.O. Box 211, Mianyang, Sichuan 621000, Peoples Republic of China;
†Department of Mechanical and Control Engineering, University of Electro-Communications, Tokyo 182, Japan

Received December 11, 1995; revised July 12, 1996

We develop here compact high-order accurate nonlinear schemes for discontinuities capturing. Such schemes achieve high-order spatial accuracy by the cell-centered compact schemes. Compact adaptive interpolations of variables at cell edges are designed which automatically ''jump'' to local ones as discontinuities being encountered. This is the key to make the overall compact schemes capture discontinuities in a nonoscillatory manner. The analysis shows that the basic principle to design a compact interpolation of variables at the cell edges is to prevent it from crossing the discontinuous data, such that the accuracy analysis based on Taylor series expanding is valid over all grid points. A high-order Runge–Kutta method is employed for the time integration. The conservative property, as well as the boundary schemes, is discussed. We also extend the schemes to a system of conservation laws. The extensions to multidimensional problems are straightforward. Some typical one-dimensional numerical examples, including the shock tube problem, strong shock waves with complex wave interactions, and ''shock/turbulence'' interaction, are presented.

1. INTRODUCTION

Although compact finite difference schemes have advantages over traditional finite difference schemes, including the relatively high-order of accuracy using a compact stencil and a better resolution for high frequency waves [1–3], the grid-to-grid oscillation was encountered as being applied to capture discontinuities due to their linear property. Harten [4] first studied this problem, but his numerical results oscillate to the point of being meaningless near discontinuity in some cases. Recently Cockburn and Shu [5] developed nonlinear compact schemes. They followed the TVD (total variation diminishing) idea with a modified limiter, such that the schemes have the so-called uniform high-order accuracy even at local extrema. The nonphysical oscillation, however, still appeared for their fourth-order scheme.

In this paper, compact high-order accurate nonlinear schemes are developed. As we know, compact schemes are global. That is, the approximation to a derivative at one grid point involves the whole line of variables. If they are applied directly to discontinuous data, the spurious oscillations are inevitable near discontinuities. In our compact schemes, compact adaptive interpolations are designed which automatically ''jump'' to local ones as discontinuities are encountered. Hence the schemes are nonlinear and Gibbs phenomenon is avoided. Two propositions have been proved, which show that in order to obtain uniformly high-order accurate compact interpolants, the interpolations of variables at cell edges should be prevented from crossing discontinuous data, such that the accuracy analysis based on the Taylor series expanding is valid over all grid points.

The organization of this paper is as follows. Section 2 presents the basic compact schemes for scalar hyperbolic conservation law, including a fourth-order compact approximation to the first derivative, the compact adaptive interpolations of variables at cell edges, the analysis of the interpolations, and the time integration. In Section 3, we discuss the boundary and near boundary algorithms and the conservative property of the schemes. The extension to Euler equations is given in Section 4. Section 5 contains numerical experiments, including solutions to a linear scalar equation with different initial conditions, the solution to Burgers equation, the shock-tube problem, interactions of blast waves, and ''shock/turbulence'' interactions by solving one-dimensional Euler equations. Concluding remarks are presented in Section 6.

2. DERIVATIONS OF THE SCHEMES

In this section we consider numerical approximations to the solution of the scalar conservation law,

$$\frac{\partial u}{\partial t} + \frac{\partial f(u)}{\partial x} = 0, \tag{1}$$

subject to the given initial condition

$$u(x, 0) = u^0(x). \tag{2}$$

We assume that the initial-value problem (IVP) (1), (2) is well-posed in the sense that the solution u depends continuously on the data (2) and that this solution is piecewise smooth, with at most a finite number of discontinuities.

0021-9991/97 $25.00

2.1. *Compact Scheme for a Derivative*

Let $u_j = u_h(x_j, t), x_j = jh$; denote a numerical approximation to the solution of Eq. (1). With a semidiscrete finite difference scheme in mind, we note that, at every node x_j, Eq. (1) can be discretized as

$$\left(\frac{\partial u}{\partial t}\right)_j = -f'_j, \tag{3}$$

where f'_j is the approximation to the space derivative. In this paper, a compact finite difference scheme for this derivative on a cell-centered mesh is used. In the fomulation presented below the nodes on which the derivative is evaluated are staggered by a half-cell ($h/2$) from the nodes on which the function values are prescribed. Such grid configurations arise naturally from a finite-volume discretization of conservation equations. As shown in [1], these cell-centered schemes have better resolution characteristics for high wave numbers than the schemes based on grid node values.

Starting from an approximation of the form

$$\kappa f'_{j-1} + f'_j + \kappa f'_{j+1} = \frac{a}{h}(\hat{f}_{j+1/2} - \hat{f}_{j-1/2}) \tag{4}$$

and matching the Taylor series up to fourth order, we obtain a fourth-order cell-centered compact scheme with the coefficients a and κ defined as

$$a = \tfrac{3}{8}(3 - 2\kappa), \quad \kappa = \tfrac{1}{22}. \tag{5}$$

The truncation error (on the r.h.s. of (4)) is $(17/5280)\, h^4\, \partial^5 f/\partial x^5$.

There are many ways to evaluate the numerical flux $\hat{f}_{j+1/2}$ at cell edge $j + \frac{1}{2}$. For example, the point values f near node j can be directly used for the interpolations at the cell edge. In this paper, however, Roe's approximate Riemann solver is used as the building block,

$$\hat{f}_{j+1/2} = \tfrac{1}{2}[f(u_{\mathrm{R}}) + f(u_{\mathrm{L}}) - |\tilde{a}|(u_{\mathrm{R}} - u_{\mathrm{L}})]_{j+1/2}, \tag{6}$$

where $\tilde{a}$ is the characteristic speed obtained by some average of u_{R} and u_{L}, such that

$$f(u_{\mathrm{R}}) - f(u_{\mathrm{L}}) = \tilde{a}(u_{\mathrm{R}} - u_{\mathrm{L}}) \tag{7}$$

is satisfied for any u_{R} and u_{L}.

When $u_{\mathrm{R}j+1/2}$ and $u_{\mathrm{L}j+1/2}$ are interpolated to rth-order accuracy such that

$$\hat{f}_{j+1/2} = f(u_{j+1/2}) + d(x_{j+1/2})h^r + O(h^{r+1}) \tag{8}$$

the resolution characteristics of the interpolation schemes when combined with those of cell-centered differentiation determine the resolution characteristics of the overall scheme.

Substituting (8) into (4) and expanding both sides of (4) in Taylor series at grid point j, we get

$$f'_j = \left(\frac{\partial f}{\partial x}\right)_j + a\,\frac{d(x_{j+1/2}) - d(x_{j-1/2})}{h}\,h^r + \frac{17}{5280}\left(\frac{\partial^5 f}{\partial x^5}\right)_j h^4 + O(h^6, h^{r+1}).$$

It is obvious that the compact scheme (4) is fourth-order accurate if $r \geq 4$ and $d(x)$ is Lipschitz continuous. In the case for $r < 4$, the scheme is rth-order accurate.

2.2. *Compact Adaptive Interpolations*

As discussed in above subsection, when $f(u)$ is a nonlinear function of u, the approximation of $\hat{f}_{j+1/2}$ to $O(h^r)$ requires knowledge of the solutions u_{R} and u_{L} to the same order of accuracy at cell edge $j + \frac{1}{2}$. We solve this problem by compact adaptive interpolations.

The basic interpolations for $u_{\mathrm{L}j+1/2}$ and $u_{\mathrm{L}j+1/2}$ are the fifth-order tridiagonal left- and right-biased compact interpolants:

$$\tfrac{1}{2}u_{\mathrm{L}j-1/2} + u_{\mathrm{L}j+1/2} + \tfrac{1}{10}u_{\mathrm{L}j+3/2} = \tfrac{1}{10}u_{j-1} + u_j + \tfrac{1}{2}u_{j+1} - \tfrac{12}{5!}h^5 + O(h^6), \tag{9}$$

$$\tfrac{1}{10}u_{\mathrm{R}j-1/2} + u_{\mathrm{R}j+1/2} + \tfrac{1}{2}u_{\mathrm{R}j+3/2} = \tfrac{1}{2}u_j + u_{j+1} + \tfrac{1}{10}u_{j+2} + \tfrac{12}{5!}h^5 + O(h^6). \tag{10}$$

The right-hand sides of the interpolants are a three point stencil and over two grid cells, i.e., I_{j-1} and I_j ($I_j = [x_j, x_{j+1}]$) for u_{L}. If a discontinuity is contained in one of these cells, the interpolant (9) will cause nonphysical oscillations. We should prevent the interpolation from crossing discontinuities, so that the following two interpolants are derived as candidates for $u_{\mathrm{L}j+1/2}$:

$$\alpha_1 u_{\mathrm{L}j-1/2} + u_{\mathrm{L}j+1/2} = a_1 u_{j-2} + b_1 u_{j-1} + c_1 u_j + \tfrac{3}{3!}(\alpha_1 - 5)h^3 + O(h^4), \tag{11}$$

if a discontinuity exists in cell I_j, and

$$u_{\mathrm{L}j+1/2} + \alpha_2 u_{\mathrm{L}j+3/2} = a_2 u_j + b_2 u_{j+1} + c_2 u_{j+2} + \tfrac{3}{3!}(\alpha_2 - 1)h^3 + O(h^4) \tag{12}$$

in case a discontinuity is contained in cell I_{j-1}. The parameters in (11), (12) will be discussed later.

The left-hand sides of (11) and (12) contain only two terms. This is the key to make the global compact interpolation a local one near discontinuities. We will also discuss this feature in the next subsection.

Thus, the task in hand is how to choose these interpolants. We solve this problem by choosing the smoothest stencil as that of ENO reconstructions [6] with some modifications. Define the first- and second-order differences

$$\begin{aligned} D_{1j} &= u_{j+1} - u_j, \\ D_{2j} &= u_{j+1} - 2u_j + u_{j-1}. \end{aligned} \tag{13}$$

The interpolants (9), (11), and (12) can be written as

$$\begin{aligned} &\tfrac{1}{2}u_{\mathrm{L}j-1/2} + u_{\mathrm{L}j+1/2} + \tfrac{1}{10}u_{\mathrm{L}j+3/2} \\ &\quad = \tfrac{16}{10}u_j + \tfrac{1}{10}(4D_{1j-1} + 5D_{2j}) \end{aligned} \tag{14}$$

or

$$= \tfrac{16}{10}u_j + \tfrac{1}{10}(4D_{1j} + D_{2j}),$$

$$\begin{aligned} &\alpha_1 u_{\mathrm{L}j-1/2} + u_{\mathrm{L}j+1/2} \\ &\quad = (1+\alpha_1)u_j + \tfrac{1}{8}[(4-4\alpha_1)D_{1j-1} + (3-\alpha_1)D_{2j-1}] \end{aligned} \tag{15}$$

$$\begin{aligned} &u_{\mathrm{L}j+1/2} + \alpha_2 u_{\mathrm{L}j+3/2} \\ &\quad = (1+\alpha_2)u_j + \tfrac{1}{8}[(12\alpha_2+4)D_{1j} + (3\alpha_2-1)D_{2j+1}]. \end{aligned} \tag{16}$$

We see that the right-hand sides of above interpolants consist of first and second differences. As we know, the absolutes of D_1, D_2 can be taken as measures of the smoothness of the stencil. The smaller the $|D_1|$ and $|D_2|$, the more smooth the "grid stencil." We choose the stencil on which $|D_1|$ and $|D_2|$ are the minimum within the cells involved. This can be finished by determining a switch function K_{L} for $u_{\mathrm{L}j+1/2}$,

$$K_{\mathrm{L}} = \begin{cases} 1, & \text{if } \beta|D_{1j-1}| \le |D_{1j}|, |D_{2j-1}| < \beta|D_{2j}|; \\ 3, & \text{if } |D_{1j}| < \beta|D_{1j-1}|, |D_{2j+1}| < \beta|D_{2j}|; \\ 2, & \text{otherwise.} \end{cases} \tag{17}$$

The interpolation for $u_{\mathrm{L}j+1/2}$ is selected as

$$\alpha_1 u_{\mathrm{L}j-1/2} + u_{\mathrm{L}j+1/2} = a_1 u_{j-2} + b_1 u_{j-1} + c_1 u_j,$$

if $K_{\mathrm{L}} = 1$;

$$\tfrac{1}{2}u_{\mathrm{L}j-1/2} + u_{\mathrm{L}j+1/2} + \tfrac{1}{10}u_{\mathrm{L}j+3/2} = \tfrac{1}{10}u_{j-1} + u_j + \tfrac{1}{2}u_{j+1}, \tag{18}$$

if $K_{\mathrm{L}} = 2$; or

$$u_{\mathrm{L}j+1/2} + \alpha_2 u_{\mathrm{L}j+3/2} = \alpha_2 u_j + b_2 u_{j+1} + c_2 u_{j+2},$$

if $K_{\mathrm{L}} = 3$.

The interpolation for $u_{\mathrm{R}j+1/2}$ is obtained in a similar manner; i.e., we first determine K_{R}:

$$K_{\mathrm{R}} = \begin{cases} 1, & \text{if } \beta|D_{1j+1}| \le |D_{1j}|, |D_{2j+2}| < \beta|D_{2j+1}|; \\ 3, & \text{if } |D_{1j}| < \beta|D_{1j+1}|, |D_{2j}| < \beta|D_{2j+1}|; \\ 2, & \text{otherwise.} \end{cases} \tag{19}$$

Then

$$u_{\mathrm{R}j+1/2} + \alpha_1 u_{\mathrm{R}j+3/2} = a_1 u_{j+3} + b_1 u_{j+2} + c_1 u_{j+1},$$

if $K_{\mathrm{R}} = 1$;

$$\tfrac{1}{10}u_{\mathrm{R}j-1/2} + u_{\mathrm{R}j+1/2} + \tfrac{1}{2}u_{\mathrm{R}j+3/2} = \tfrac{1}{2}u_j + u_{j+1} + \tfrac{1}{10}u_{j+2}, \tag{20}$$

if $K_{\mathrm{R}} = 2$; or

$$\alpha_2 u_{\mathrm{R}j-1/2} + u_{\mathrm{R}j+1/2} = a_2 u_{j+1} + b_2 u_j + c_2 u_{j-1},$$

if $K_{\mathrm{R}} = 3$.

The parameters in above interpolants are given by

$$\begin{aligned} &a_1 = (3-\alpha_1)/8, b_1 = (6\alpha_1 - 10)/8, c_1 = (3\alpha_1 + 15)/8; \\ &a_2 = (3-\alpha_2)/8, b_2 = (6+6\alpha_2)/8, c_2 = (3\alpha_2 - 1)/8, \end{aligned} \tag{21}$$

except the parameter β. We take $0 \le \beta \le 1$ in order that the basic interpolation (9) and (10) are used as many as possible. If $\beta = 0$, the fifth-order interpolations (9) and (10) being used at all grid points, a linear fourth-order scheme is recovered which can be used for problems free of discontinuities. We found $\beta = 0.5$ works well in most of our numerical experiments given in Section 5.

The above interpolation is third-order accurate as $\alpha_1 \neq$

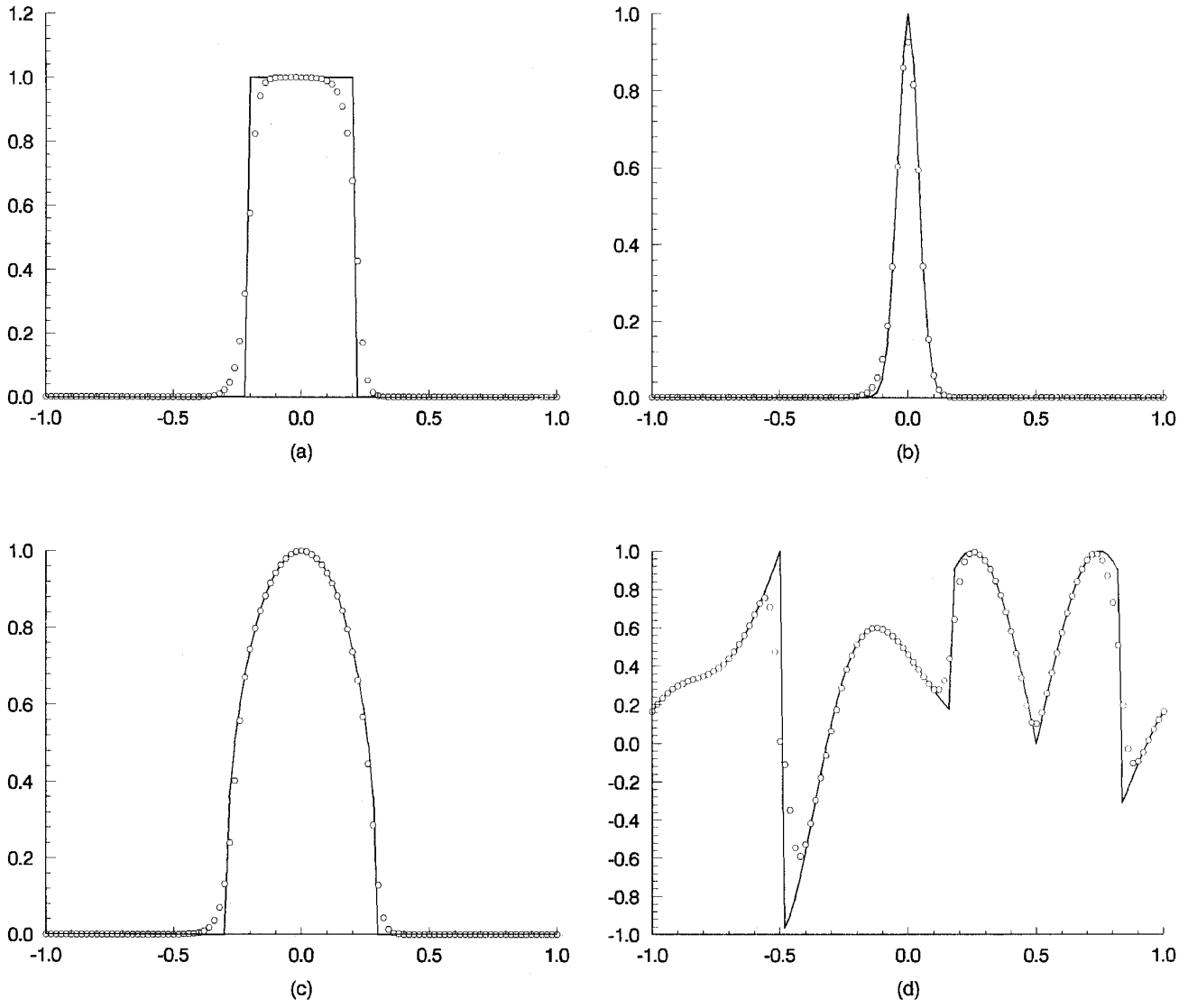

FIG. 1. Numerical solutions of linear equation with different initial conditions.

5 and $\alpha_2 \neq 1$. The numerical flux (6), together with the above adaptive interpolations, is third-order accurate,

$$\hat{f}_{j+1/2} = f(u_{j+1/2}) + O(h^3), \tag{22}$$

and the final accuracy of space derivative in Eq. (3) is third order also.

It is obvious from (11), (12) that if $\alpha_1 = 5$ and $\alpha_2 = 1$, the interpolations are fourth-order accurate. Unfortunately, these parameters cannot be used in practice, for the inversion of the tridiagonal matrix equations (27) requires the diagonal elements be dominant; i.e., $\alpha_1 < 1$ and $\alpha_2 < 1$. In order to get fourth-order accurate interpolations, we have to add one point value on either side of the interpolants (11), (12). If being added in the left-hand side, we need to invert a pentadigonal matrix (which will be discussed in our next paper). In this paper, we simply add one point on the right-hand side; i.e., u_{j-3} is added in (11) and u_{j+3} is added in (12). Hence a fourth-order interpolation is obtained,

$$\alpha_3 u_{\mathrm{L}j-1/2} + u_{\mathrm{L}j+1/2} = a_3 u_{j-3} + b_3 u_{j-2} + c_3 u_{j-1} + d_3 u_j,$$

if $K_{\mathrm{L}} = 1$;

$$\tfrac{1}{2} u_{\mathrm{L}j-1/2} + u_{\mathrm{L}j+1/2} + \tfrac{1}{10} u_{\mathrm{L}j+3/2} = \tfrac{1}{10} u_{j-1} + u_j + \tfrac{1}{2} u_{j+1}, \tag{23}$$

if $K_{\mathrm{L}} = 2$; or

$$u_{\mathrm{L}j+1/2} + \alpha_4 u_{\mathrm{L}j+3/2} = \alpha_4 u_j + b_4 u_{j+1} + c_4 u_{j+2} + d_4 u_{j+3},$$

if $K_{\mathrm{L}} = 3$;

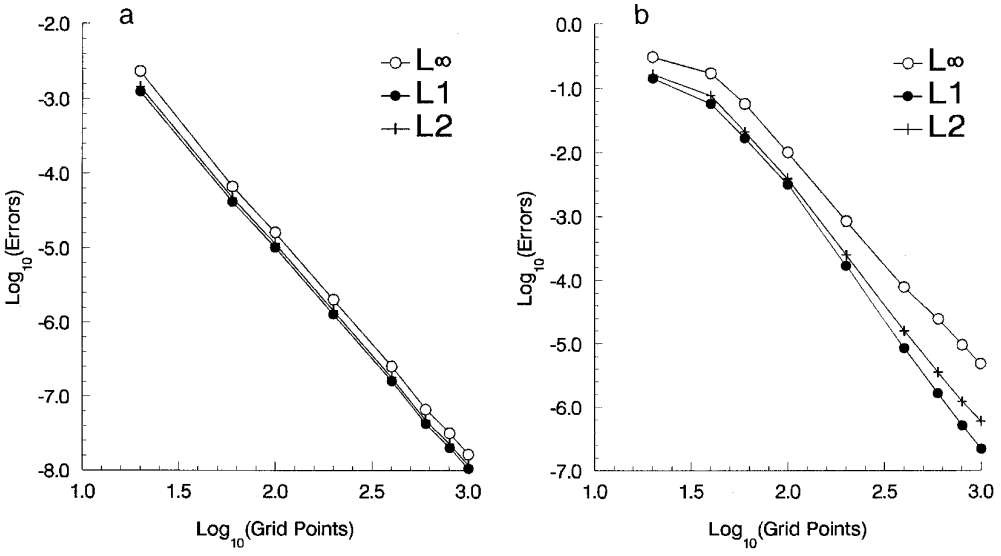

FIG. 2. L_∞, L_1, and L_2 errors as a function of grid point number. T = 2, CFL = 0.4: (a) $u_0 = \sin(2\pi x)$; (b) $u_0 = \sin^4(2\pi x)$.

the interpolation for $u_{\mathrm{R}j+1/2}$ is modified in the same way,

$$u_{\mathrm{R}j+1/2} + \alpha_3 u_{\mathrm{R}j+3/2} = a_3 u_{j+4} + b_3 u_{j+3} + c_3 u_{j+2} + d_3 u_{j+1},$$

if $K_{\mathrm{R}} = 1$;

$$\tfrac{1}{10} u_{\mathrm{R}j-1/2} + u_{\mathrm{R}j+1/2} + \tfrac{1}{2} u_{\mathrm{R}j+3/2} = \tfrac{1}{2} u_j + u_{j+1} + \tfrac{1}{10} u_{j+2}, \tag{24}$$

if $K_{\mathrm{R}} = 2$; or

$$\alpha_4 u_{\mathrm{R}j-1/2} + u_{\mathrm{R}j+1/2} = a_4 u_{j+1} + b_4 u_j + c_4 u_{j-1} + d_4 u_{j-2},$$

if $K_{\mathrm{R}} = 3$,

where

$$a_3 = (\alpha_3 - 5)/16, \qquad b_3 = (21 - 5\alpha_3)/16,$$
$$c_3 = (15\alpha_3 - 35)/16, \qquad d_3 = (5\alpha_3 + 35)/16;$$
$$a_4 = (5 - \alpha_4)/16, \qquad b_4 = (15 + 9\alpha_4)/16,$$
$$c_4 = (9\alpha_4 - 5)/16, \qquad d_4 = (1 - \alpha_4)/16$$

with $\alpha_3 < 1$ and $\alpha_4 < 1$. The numerical flux is fourth-order accurate,

$$\hat{f}_{j+1/2} = f(u_{j+1/2}) + O(h^4) \tag{25}$$

and a fourth-order accurate scheme is obtained.

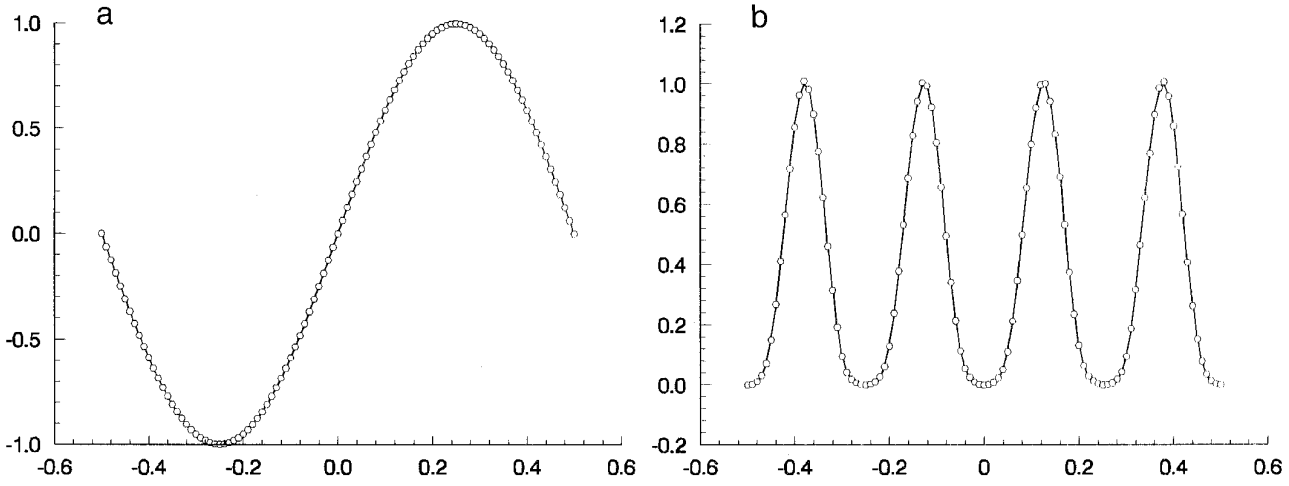

FIG. 3. Numerical solutions of linear equation with (a) $u_0 = \sin(2\pi x)$, (b) $u_0 = \sin^4(2\pi x)$.

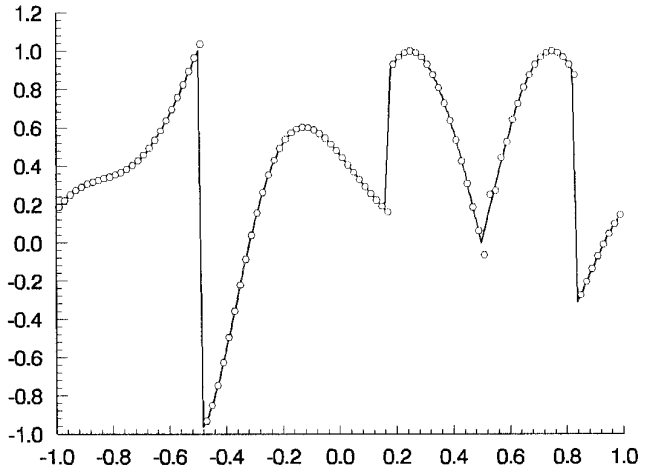

FIG. 4. The result of compact interpolation for $u_{Lj+1/2}$.

It should be pointed out that at some grid points above compact adaptive interpolations will result in $d(x)$ in (8) failing to be Lipschitz continuous, such that the accuracy will be one order lower at these points. We expect the number of these points to remain bounded as $h \to 0$.

2.3. *Analysis of the Compact Adaptive Interpolations*

The principle of designing our compact adaptive interpolation is that the interpolants do not cross discontinuities, such that the accuracy analysis based on Taylor series expansion is valid over all grid points. In other words, one reason for nonphysical oscillation caused by fixed stencil interpolation is that the Taylor series expansion is applied for the discontinuous data. We will prove that our compact adaptive interpolations do not encounter this problem and have uniform high-order accuracy.

Let $q(x_{j+1/2}; v(x))$ denote the left-state third-order compact adaptive interpolant of $v(x)$ at $x_{j+1/2}$ and $[x_{j_{\min}}, ..., x_{j_{\max}}]$ denote the interval of the right-hand side of the interpolation. There are two cases which should be considered.

PROPOSITION 2.1. *For any piecewise smooth $v(x)$, possibly having jump discontinuities, there exists an $h_0 > 0$, such that, for all $h \le h_0$ and all j,*

$$q(x_{j+1/2}; v(x)) = v(x_{j+1/2}) + O(h^3). \tag{26}$$

Proof. Consider the interval $x_j \le x \le x_{j+1}$ and the interpolation at cell edge $x_{j+1/2}$. If v is smooth over the full interval of interpolation $[x_{j_{\min}}, ..., x_{j_{\max}}]$ standard interpolation results imply $q = v + O(h^3)$. If a single discontinuity exists in the interval $x_j \le x \le x_{j+1}$, such that the differences D_{1j}, D_{2j}, and D_{2j+1} are very much larger than those of neighbor grid points, the definition of $q(x_{j+1/2}, v)$ guarantees that the compact adaptive interpolation has the following tri-digonal matrix form:

$$\begin{bmatrix} 1 & \alpha_2 & & & & & \\ \ddots & \ddots & \ddots & & & & \\ & \alpha_1 & 1 & & & & \\ & & & 1 & \alpha_2 & & \\ & & & \ddots & \ddots & \ddots & \end{bmatrix} \begin{bmatrix} u_{L3/2} \\ \vdots \\ u_{Lj+1/2} \\ u_{Lj+3/2} \\ \vdots \end{bmatrix}$$

$$= \begin{bmatrix} a_2 & b_2 & c_2 & & & & \\ \ddots & \ddots & \ddots & \ddots & & & \\ & a_1 & b_1 & c_1 & & & \\ & & & & a_2 & b_2 & c_2 \\ & & & & \ddots & \ddots & \ddots & \ddots \end{bmatrix} \begin{bmatrix} u_1 \\ \vdots \\ u_{j-1} \\ u_j \\ u_{j+1} \\ \vdots \end{bmatrix}. \tag{27}$$

Hence the values of interpolations, $(u_{1/2}, ..., u_{j+1/2})$ and $(u_{1/2}, ..., u_{j+1/2})$, are independent of each other, and the global compact interpolation is divided into two local parts by the discontinuity. In every part, the Taylor series expansion is valid, which guarantees that $q = v + O(h^3)$.

In the case that there are several divided jump discontinuities, if h_0 is small enough, such that there are enough grid points between discontinuities, the above proof is valid also. ∎

Of course, the interval of interpolation, $[x_{j_{\min}}, ..., x_{j_{\max}}]$, may contain discontinuities, which may be encountered in two situations. One is that a discontinuity is too weak numerically, for example, at the initial stage of the shock wave generation, such that $|D_1|$ and $|D_2|$ are smaller than those of smooth regions. Another is that a grid point, for example x_j, is attached at a "discontinuity." The discontinuity for the former situation can be treated numerically as a smooth region and would not cause much oscillation due to its weakness. The latter case is usually encountered in the numerical calculations, which should be analyzed in detail. As we know, a numerical solution is only an approximated one. If a jump discontinuity is simulated numerically as a region with a very sharp gradient, for example, one grid point attached at the discontinuity, it can be taken as a correct analogy to the mathematical discontinuity. Based on this consideration, we have

PROPOSITION 2.2. *For any smooth $v(x)$, possibly having monotone regions with very strong gradient (analogous to numerical jump discontinuities), there exists an $h_0 > 0$, such that, for all $h \le h_0$ and all j,*

$$q(x_{j+1/2}; v(x)) = v(x_{j+1/2}) + O(h^3). \tag{28}$$

Proof. Assume the interval $x_{j-1} \le x \le x_{j+1}$ is a single monotone region with a very strong gradient and x_{j-1} and x_{j+1} are its edges. This is an analogy of a numerical discontinuity with one grid point x_j attached. Consider the left-state interpolation at $x_{j-1/2}$, $x_{j+1/2}$, and $x_{j-3/2}$. By the assumption we know that $|D_{1j-1}|$, $|D_{1j}$, $|D_{2j-1}|$, and $|D_{2j+1}|$, are larger than those of neighbor grid points. Hence, the compact adaptive interpolation must have the following matrix form:

$$\begin{bmatrix} 1 & \alpha_2 & & & & & & \\ \ddots & \ddots & \ddots & & & & & \\ & \alpha_1 & 1 & & & & & \\ & & \frac{1}{2} & 1 & \frac{1}{10} & & & \\ & & & & 1 & \alpha_2 & & \\ & & & & \ddots & \ddots & \ddots & \end{bmatrix} \begin{bmatrix} u_{\mathrm{L}3/2} \\ \vdots \\ u_{\mathrm{L}j-1/2} \\ u_{\mathrm{L}j+1/2} \\ u_{\mathrm{L}j+3/2} \\ \vdots \end{bmatrix}$$

$$= \begin{bmatrix} a_2 & b_2 & c_2 & & & & & & \\ \ddots & \ddots & \ddots & \ddots & & & & & \\ & a_1 & b_1 & c_1 & & & & & \\ & & & \frac{1}{10} & 1 & \frac{1}{2} & & & \\ & & & & & a_2 & b_2 & c_2 & \\ & & & & & \ddots & \ddots & \ddots & \ddots \end{bmatrix} \begin{bmatrix} u_1 \\ \vdots \\ u_{j-2} \\ u_{j-1} \\ u_j \\ u_{j+1} \\ \vdots \end{bmatrix}. \tag{29}$$

We can see that the interpolation is divided into three local regions. The interpolations in domains $[x_{3/2}, ..., x_{j-1/2}]$ and $[x_{j+3/2}, ..., x_{N-1/2}]$ do not cross the very strong gradient region $[x_{j-1}, x_{j+1}]$, the same as Proposition 2.1; thus $q = v + O(h^3)$ holds in all these three regions.

If one more grid point is contained in the very strong gradient region, it can be proved in the same way. ∎

The fourth-order interpolant (23)–(24) has the same structure as the third-order one, so the uniform high-order accuracy is also expected as the numerical examples in Section 5 shown.

2.4. *Time Discretization*

We treat (3) as an ordinary differential equation for the purpose of time discretization, using a "method-of-line" approach. Along any t = constant line, the right-hand side of (3) is strictly a spatial operation in u, and we rewrite this equation, for fixed t, in the abstract operator-product form

$$\frac{\partial u}{\partial t} = L(u), \tag{30}$$

thus effectively "separating" the spatial and temporal operations for computing solutions of (1).

In [7], Runge–Kutta methods are presented for the time discretization of ordinary differential equations which are of high-order accurate and total-variation diminishing (TVD), in the sense that the temporal operator itself does not increase the total variation of the solution. The third-order one of these Runge–Kutta methods is employed in this paper that reads

$$\begin{aligned} u^{(1)} &= u^n + \Delta t L(u^n) \\ u^{(2)} &= \tfrac{3}{4}u^n + \tfrac{1}{4}u^{(1)} + \tfrac{1}{4}\Delta t L(u^{(1)}) \\ u^{n+1} &= \tfrac{1}{3}u^n + \tfrac{2}{3}u^{(2)} + \tfrac{2}{3}\Delta t L(u^{(2)}) \end{aligned} \tag{31}$$

with CFL ≤ 1.

There are also fourth- and fifth-order versions with some technical complexity [7].

Remark. It is difficult at present to prove theoretically the convergence of the numerical solutions due to the nonlinearity of schemes. We resort to the numerical examples to test their performance in Section 5.

3. BOUNDARY SCHEMES AND CONSERVATIVE FORMULATION FOR THE FIRST DERIVATIVE

A natural consequence of using compact scheme (4) is that the boundary and near boundary grid points may require special procedures to compute the derivatives, as well as the left and right state interpolations. These approximations are, of necessity, one-sided. In the description below, $j = 1$ and $j = N$ represent the left and right boundary points. We follow the way that is widely used in the traditional finite difference schemes, i.e., calculating the derivatives at interior points (2, 3, ..., $N-2$, $N-1$), and interpo-

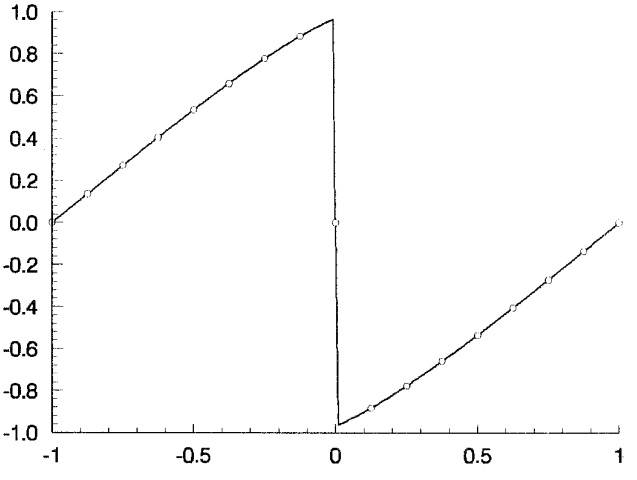

FIG. 5. Numerical solution of Burgers equations.

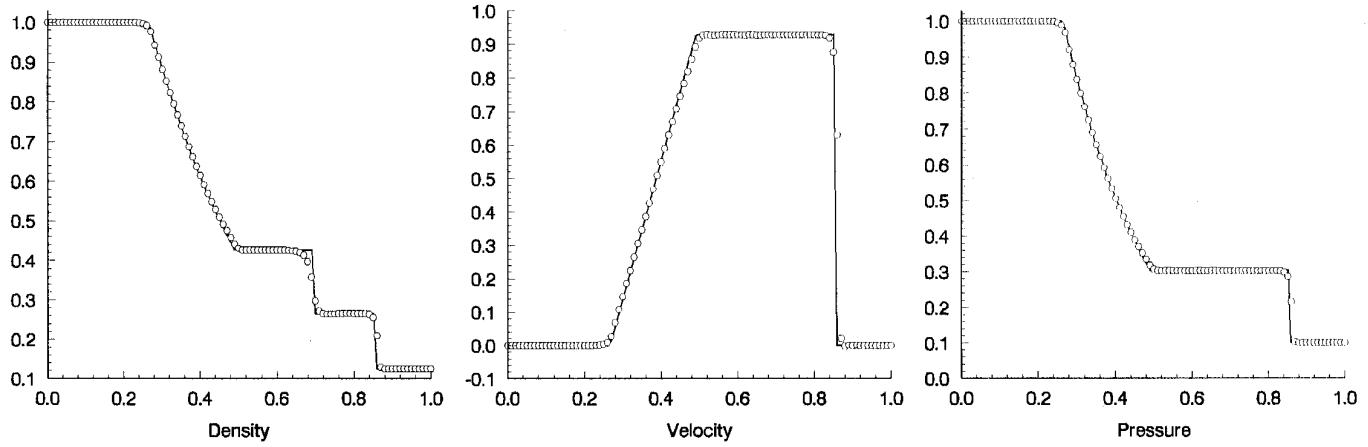

FIG. 6. Numerical solutions of Sod problem.

lating or specifying the values at the boundary points $j = 1$ and $j = N$.

The first derivative at the near boundary point $j = 2$ and $j = N - 1$ may be obtained by

$$f'_2 + \kappa_1 f'_3 = \frac{1}{\mathrm{h}}(a_1 \hat{f}_{3/2} + b_1 \hat{f}_{5/2} + c_1 \hat{f}_{7/2}) \tag{32}$$

$$f'_{N-1} + \kappa_2 f'_{N-2} = \frac{1}{\mathrm{h}}(a_2 \hat{f}_{N-1/2} + b_2 \hat{f}_{N-3/2} + c_2 \hat{f}_{N-5/2}), \tag{33}$$

where

$$a_1 = -1, \quad b_1 = 1 - \kappa_1, \qquad c_1 = \kappa_1;$$
$$a_2 = 1, \qquad b_2 = 1 - (1 - \kappa_2), \quad c_2 = -\kappa_2.$$

If $\kappa_1 = \kappa_2 = -1$, they are third-order accurate.

The variables at the near boundary cell edges can be obtained by fixed stencil interpolations that involve the pointwise variables available.

An important requirement in developing high-order approximation to the spactial derivatives is the global conservation property. Lele [1] discussed this problem for compact schemes. We follow his way to give an approach for constructing difference approximation of our schemes at the near boundary points which satisfy a discrete form of global conservation constraints.

Integrating (1) over the domain $[a, b]$ yields

$$\frac{d}{dt}\int_{x=a}^{x=b} u(x,t)dx = f|_{(x=a,t=t)} - f|_{(x=b,t=t)}, \tag{34}$$

showing that the total u in the domain changes only due to the flux of u at the boundary. This is a global conservation statement. We seek a formulation for the near boundary points such that the global conservation law (34) has a discrete analogy for the difference approximations.

We write the scheme (4) in matrix form,

$$\mathbf{A}\mathbf{f}' = \frac{1}{\mathrm{h}}\mathbf{B}\hat{\mathbf{f}}, \tag{35}$$

$$\mathbf{A} = \begin{bmatrix} w_1 & w_1\kappa_1 & & & & \\ w_2\kappa & w_2 & w_2\kappa & & & \\ & \kappa & 1 & \kappa & & \\ & & \kappa & 1 & \kappa & \\ & & & \ddots & \ddots & \ddots \end{bmatrix},$$

$$\mathbf{B} = \begin{bmatrix} w_1 a_1 & w_1 b_1 & w_1 c_1 & & & \\ & -w_2 a & w_2 a & & & \\ & & -a & a & & \\ & & & -a & a & \\ & & & & \ddots & \ddots \end{bmatrix},$$

and $\mathbf{f}'$, $\hat{\mathbf{f}}$ are $N - 2$, $N - 1$ vectors, respectively. Two weights, w_1 and w_2, are introduced at near boundary points. In order to satisfy the global conservation constraint it is sufficient to require that columns 2 through $N - 2$ of the matrix $\mathbf{B}$ sum exactly to zero. This ensures that only the boundary points contribute to the near boundary flux. Thus the weights w_1 and w_2 are determined as

$$w_1 = a, \quad w_2 = 1 - \kappa_1.$$

Another near boundary point, $N - 1$, can be treated in a similar manner.

Remark. If inverse boundary conditions can be used in calculations, the boundary formulation is simple, for we know

$$f'_0 = cf'_2, \tag{36}$$

where c is a constant and may be determined by inverse boundary conditions. By inserting (36) into (4), the tridiagonal matrix is solvable. This treatment is used in the solutions of the Euler equation in Section 5.

4. THE EXTENSION TO THE EULER EQUATIONS OF GAS DYNAMICS

A special advantage of our schemes, as well as finite difference ENO schemes [7, 8], is their relative simplicity in multidimensional problems. The schemes developed in Sections 2, 3 can be applied in each dimension individually, keeping all other variables fixed. Thus, in this section we only describe how to extend these schemes to one dimensional Euler equations of gas dynamics. The extensions to multidimensional problems are straightforward.

For a polytropic gas, the governing equations are

$$\frac{\partial U}{\partial t} + \frac{\partial F}{\partial x} = 0 \tag{37}$$

with

$$U = [\rho, \rho u, e]^{\mathrm{T}},$$
$$F = [\rho u, \rho u^2 + p, (e + p)u]^{\mathrm{T}},$$
$$p = (\gamma - 1)(e - \tfrac{1}{2}\rho u^2).$$

Here ρ, u, p, and e are the density, velocity, pressure, and total energy respectively; γ is the ratio of specific heats.

The eigenvalues of the Jacobian matrix $\partial F/\partial U$ are

$$\lambda^1 = u - c, \quad \lambda^2 = u, \quad \lambda^3 = u + c, \tag{38}$$

where $c = (\gamma p/\rho)^{1/2}$ is the sound speed.

The corresponding right-eigenvectors are

$$r^1 = \begin{pmatrix} 1 \\ u - c \\ H - uc \end{pmatrix}, \quad r^2 = \begin{pmatrix} 1 \\ u \\ \frac{1}{2}u^2 \end{pmatrix}, \quad r^3 = \begin{pmatrix} 1 \\ u + c \\ H + uc \end{pmatrix}; \tag{39}$$

here

$$H = \frac{e + p}{\rho} = \frac{c^2}{\gamma - 1} + \frac{1}{2}u^2 \tag{40}$$

is the enthalpy.

The corresponding left-eigenvectors bi-orthonormal to (39) are

$$\begin{aligned} l^1 &= \tfrac{1}{2}(b_2 + u/c, -b_1 u - 1/c, b_1), \\ l^2 &= \tfrac{1}{2}(1 - b_2, b_1 u, -b_1), \\ l^3 &= \tfrac{1}{2}(b_2 - u/c, -b_1 u + 1/c, b_1), \end{aligned} \tag{41}$$

where

$$\begin{aligned} b_1 &= (\gamma - 1)/c^2 \\ b_2 &= \tfrac{1}{2}u^2 b_1. \end{aligned} \tag{42}$$

Roe's approximate Riemann solver,

$$\hat{F}_{j+1/2} = \tfrac{1}{2}[F(U_{\mathrm{R}}) + F(U_{\mathrm{L}}) - |\tilde{A}|(U_{\mathrm{R}} - U_{\mathrm{L}})]_{j+1/2}, \tag{43}$$

is also applied to get the derivatives $\partial F/\partial x$ in (4). Where $\tilde{A}$ is calculated by Roe's averages of U_{L} and U_{R},

$$\begin{aligned} \tilde{u} &= (u_{\mathrm{L}} + u_{\mathrm{R}}\sqrt{\rho_{\mathrm{R}}/\rho_{\mathrm{L}}})/(1 + \sqrt{\rho_{\mathrm{R}}/\rho_{\mathrm{L}}}) \\ \tilde{H} &= (H_{\mathrm{L}} + H_{\mathrm{R}}\sqrt{\rho_{\mathrm{R}}/\rho_{\mathrm{L}}})/(1 + \sqrt{\rho_{\mathrm{R}}/\rho_{\mathrm{L}}}) \\ \tilde{c} &= (\gamma - 1)^{1/2}\sqrt{\tilde{H} - \tfrac{1}{2}\tilde{u}^2}. \end{aligned} \tag{44}$$

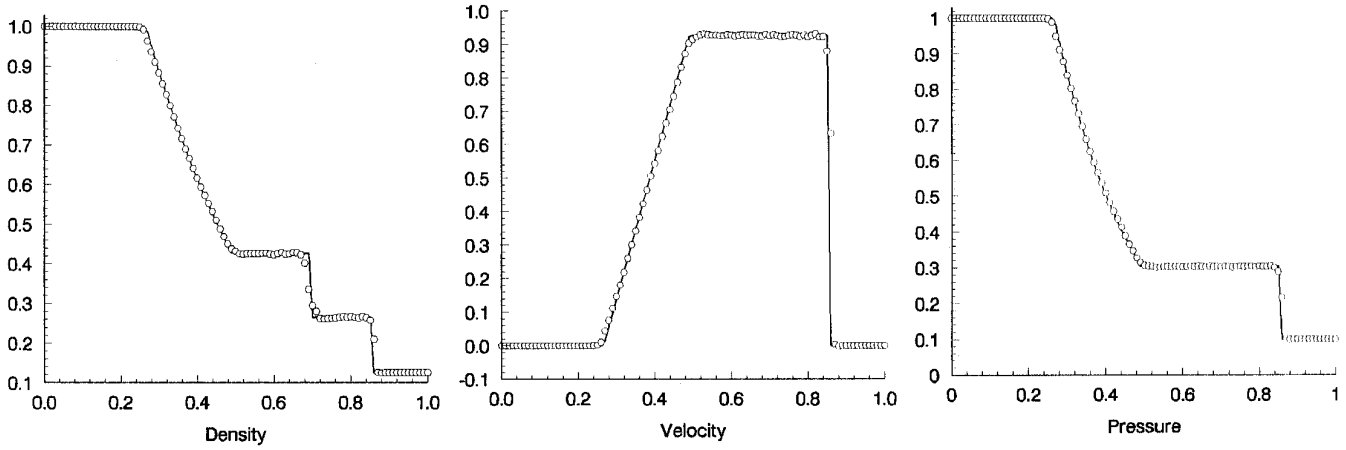

FIG. 7. Numerical solutions of Sod problem (component-wise interpolation).

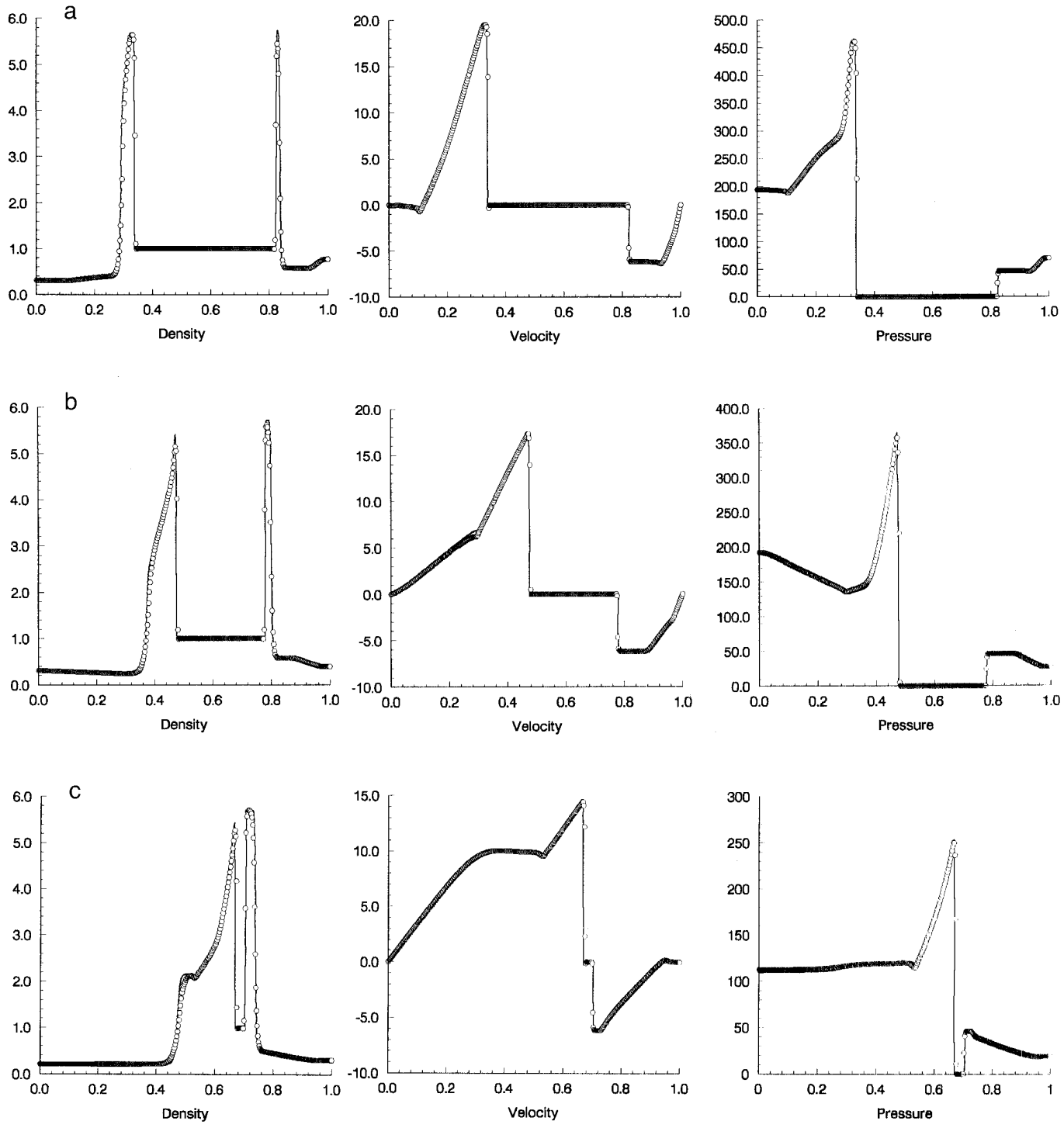

FIG. 8. Numerical solutions of interaction blast waves: (a) T = 0.010; (b) T = 0.016; (c) T = 0.026; (d) T = 0.028; (e) T = 0.030; (f) T = 0.032; (g) T = 0.034; (h) T = 0.038.

The cell-edge values, $U_{Lj+1/2}$ and $U_{Rj+1/2}$, can be obtained from (17)–(24) by interpolation of the components of U. These componentwise interpolations are simple and efficient, although not suitable, as the discontinuities collide [6].

To avoid too many collisions of the discontinuities, we may adopt the characteristic interpolations in the calculations. The variables $U_{Lj+1/2}$ and $U_{Rj+1/2}$ are decomposed into three locally defined scalar characteristic variables,

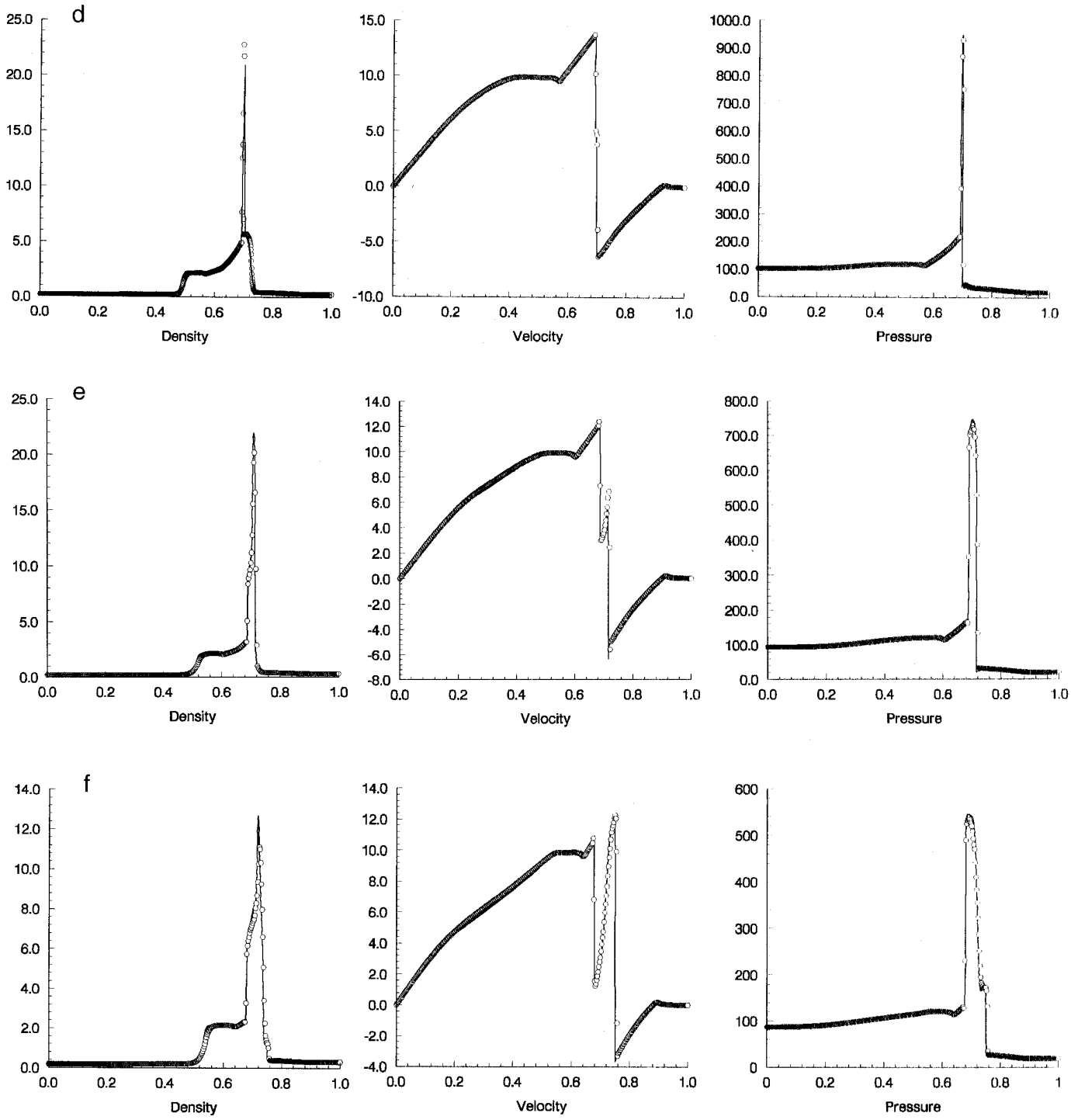

FIG. 8—*Continued*

$$U_{\mathrm{L}j+1/2} = \sum_{p=1}^{3} (l_j^p \cdot U_{\mathrm{L}j+1/2}^p) r_j^p \tag{45}$$

$$U_{\mathrm{R}j+1/2} = \sum_{p=1}^{3} (l_{j+1}^p \cdot U_{\mathrm{R}j+1/2}^p) r_{j+1}^p \tag{46}$$

using the usual l^2 inner product. The variables $U_{\mathrm{L}j+1/2}^p$ are interpolated from (17), (18) (third-order) or (17), (23) (fourth-order) with the exception that u, D_{1j}, and D_{2j} are replaced by $U, l_{i(\mathrm{L}j+1/2)}^p \cdot D_{1j}$, and $l_{i(\mathrm{L}j+1/2)}^p \cdot D_{2j}$, respectively. And we interpolate $U_{\mathrm{R}j+1/2}^p$ by (19), (20) or (19), (24),

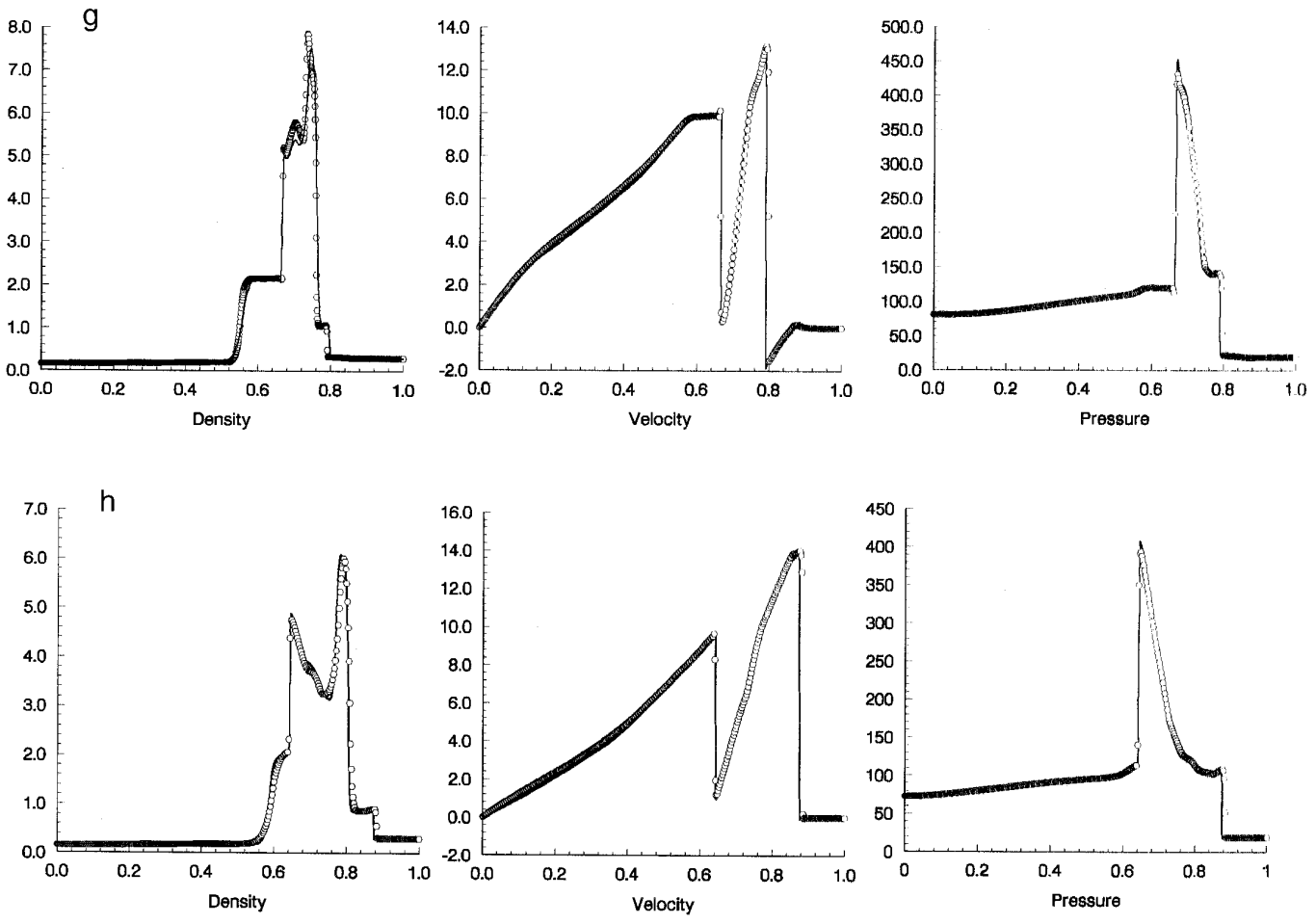

FIG. 8—*Continued*

except that u, D_{1j} and D_{2j} are replaced by U, $l^p_{i(\mathrm{R}j+1/2)} \cdot D_{1j}$, and $l^p_{i(\mathrm{R}j+1/2)} \cdot D_{2j}$, respectively. Where the subscripts, $i(Lj + 1/2)$ and $i(Rj + 1/2)$, are functions of cell-edge nodes. We take $i(Lj + 1/2) = j$ and $i(Rj + 1/2) = j + 1$ for the left- and right-biased consideration. For example, the third-order interpolations of $U^p_{\mathrm{L}j+1/2}$ and $U^p_{\mathrm{R}j+1/2}$ read

$$K_{\mathrm{L}} = \begin{cases} 1, & \text{if } \beta|l^p_{i(\mathrm{L}j+1/2)} \cdot D_{1j-1}| \le |l^p_{i(\mathrm{L}j+1/2)} \cdot D_{1j}|, \\ & |l^p_{i(\mathrm{L}j+1/2)} \cdot D_{2j-1}| < \beta|l^p_{i(\mathrm{L}j+1/2)} \cdot D_{2j}|; \\ 3, & \text{if } \beta|l^p_{i(\mathrm{L}j+1/2)} \cdot D_{1j}| < \beta|l^p_{i(\mathrm{L}j+1/2)} \cdot D_{1j-1}|, \\ & |l^p_{i(\mathrm{L}j+1/2)} \cdot D_{2j+1}| < \beta|l^p_{i(\mathrm{L}j+1/2)} \cdot D_{2j}|; \\ 2, & \text{otherwise;} \end{cases} \quad (47)$$

$$\alpha_1 U^p_{\mathrm{L}j-1/2} + U^p_{\mathrm{L}j+1/2} = a_1 U_{j-2} + b_1 U_{j-1} + c_1 U_j,$$

if $K_{\mathrm{L}} = 1$;

$$\tfrac{1}{2} U^p_{\mathrm{L}j-1/2} + U^p_{\mathrm{L}j+1/2} + \tfrac{1}{10} U^p_{\mathrm{L}j+3/2} = \tfrac{1}{10} U_{j-1} + U_j + \tfrac{1}{2} U_{j+1}, \quad (48)$$

if $K_{\mathrm{L}} = 2$; or

$$U^p_{\mathrm{L}j+1/2} + \alpha_2 U^p_{\mathrm{L}j+3/2} = \alpha_2 U_j + b_2 U_{j+1} + c_2 U_{j+2},$$

if $K_{\mathrm{L}} = 3$;

$$K_{\mathrm{R}} = \begin{cases} 1, & \text{if } \beta|l^p_{i(\mathrm{R}j+1/2)} \cdot D_{1j+1}| \le |l^p_{i(\mathrm{R}j+1/2)} \cdot D_{1j}|, \\ & |l^p_{i(\mathrm{R}j+1/2)} \cdot D_{2j+2}| < \beta|l^p_{i(\mathrm{R}j+1/2)} \cdot D_{2j+1}|; \\ 3, & \text{if } |l^p_{i(\mathrm{R}j+1/2)} \cdot D_{1j}| < \beta|l^p_{i(\mathrm{R}j+1/2)} \cdot D_{1j+1}|, \\ & |l^p_{i(\mathrm{R}j+1/2)} \cdot D_{2j}| < \beta|l^p_{i(\mathrm{R}j+1/2)} \cdot D_{2j+1}|; \\ 2, & \text{otherwise;} \end{cases} \quad (49)$$

$$U^p_{\mathrm{R}j+1/2} + \alpha_1 U^p_{\mathrm{R}j+3/2} = a_1 U_{j+3} + b_1 U_{j+2} + c_1 U_{j+1},$$

if $K_{\mathrm{R}} = 1$;

$$\tfrac{1}{10} U^p_{\mathrm{R}j-1/2} + U^p_{\mathrm{R}j+1/2} + \tfrac{1}{2} U^p_{\mathrm{R}j+3/2} = \tfrac{1}{2} U_j + U_{j+1} + \tfrac{1}{10} U_{j+2}, \quad (50)$$

if $K_{\mathrm{R}} = 2$; or

$$\alpha_2 U^p_{\mathrm{R}j-1/2} + U^p_{\mathrm{R}j+1/2} = a_2 U_{j+1} + b_2 U_j + c_2 U_{j-1},$$

if $K_{\mathrm{R}} = 3$.

5. NUMERICAL TESTS

To test the behavior of the schemes developed in the above sections, we applied them to several examples. The fourth-order scheme is used in Examples 1–3 with $\alpha_3 = \alpha_4 = 0.5$ and $\beta = 0.5$ for Examples 1–2 and $\alpha_3 = \alpha_4 = 0$, $\beta = 0.5$ for Example 3. The third-order scheme is employed in the last two examples.

EXAMPLE 1. We solve the linear equation

$$u_t + u_x = 0, \qquad -1 \le x \le 1, \tag{51}$$
$$u(x, 0) = u^0(x), \quad u^0(x) \text{ with period 2.}$$

Four initial conditions $u^0(x)$. The first three are used by Zalesak [10], using 100 equally spaced grid points in [1, 1] with

$$u^0(x) = \begin{cases} 1, & -\frac{1}{5} \le x \le \frac{1}{5}, \\ 0, & \text{otherwise;} \end{cases} \tag{52}$$

$$u^0(x) = e^{-300x^2}; \tag{53}$$

$$u^0(x) = \begin{cases} (1 - (\frac{10}{3}x)^2)^{1/2}, & |x| < \frac{3}{10}, \\ 0, & \text{otherwise.} \end{cases} \tag{54}$$

The fourth is used by Harten *et al.* [6]:

$$u^0(x + 0.5) = \begin{cases} -x \sin(\frac{3}{2}\pi x^2), & -1 \le x < -\frac{1}{3}, \\ |\sin(2\pi x)|, & |x| < \frac{1}{3}, \\ 2x - 1 - \sin(3\pi x)/6, & \frac{1}{3} < x < 1. \end{cases} \tag{55}$$

We take CFL = 0.4 in this example Figs. 1a–d show solutions at $t = 2$. From these figures we see that the scheme develops accurate solutions in the smooth regions and captures the discontinuities in a nonoscillatory manner, except for a little smearing. No special techniques to sharpen these discontinuities are used in the calculations.

In order to see the convergence rate of the schemes in smooth regions, we show the error convergence rates with mesh refreshment in Figs. 2a–b with smooth initial conditions:

$$u^0(x) = \sin(2\pi x) \tag{56}$$
$$u^0(x) = \sin^4(2\pi x). \tag{57}$$

We see that all errors monotonically decrease with the mesh size. Figures 3a–b show the solutions in $[-0.5, 0.5]$ at $t = 2$ with 100 grid points.

In Fig. 4, the result of the fourth-order compact interpolant for $u_{Lj+1/2}$ is given.

EXAMPLE 2. The Burgers equation is solved in this example:

$$u_t + \left(\frac{u^2}{2}\right)_x = 0 \tag{58}$$
$$u(x, 0) = \sin(\pi x + \pi). \tag{59}$$

For this nonlinear problem, a stationary shock is generated at $t = 1/\pi$. The numerical solution with 16 grid points and CFL = 0.5 at $t = 0.6$ is shown in Fig. 5. The shock is also captured nonoscillatorily.

EXAMPLE 3. The Riemann problem for the Euler equations of gas dynamics is solved with the initial conditions (Sod problem [11]):

$$(\rho_L, u_L, p_L) = (1, 0, 1), \quad (\rho_R, u_R, p_L) = (0.125, 0, 0.1). \tag{60}$$

In this calculation we used the characteristic interpolations with 100 grid points, CFL = 0.2, and 200 time steps. The results are given in Fig. 6. Compared with the results [8, 9] calculated by ENO schemes, our resolution of the corners of rarefaction waves (discontinuities in derivatives) are improved.

In Fig. 7 we repeat the calculation in Fig. 6 with component-wise interpolation that is simpler and much more efficient than characteristic interpolation. Some "noises" appear in Fig. 7 which, however, may be considered acceptable for practical calculations.

EXAMPLE 4. These are the same equations as in Example 3 with the initial conditions

$$U^0(x) = \begin{cases} U_L, & 0 \le x < 0.1, \\ U_M, & 0.1 \le x < 0.9, \\ U_R, & 0.9 \le x < 1, \end{cases} \tag{61}$$

where

$$\rho_L = \rho_M = \rho_R = 1, \quad u_L = u_M = u_R = 0,$$
$$p_L = 10^3, \quad p_M = 10^{-2}, \quad p_R = 10^2.$$

A solid boundary condition is applied to both ends; see [12] for details.

In this example the shock waves are very strong and complicated interactions of various waves are encountered as discussed in [12]. The third-order accurate scheme is used to solve this problem with $\alpha_1 = \alpha_2 = 0$, $\beta = 1$, and

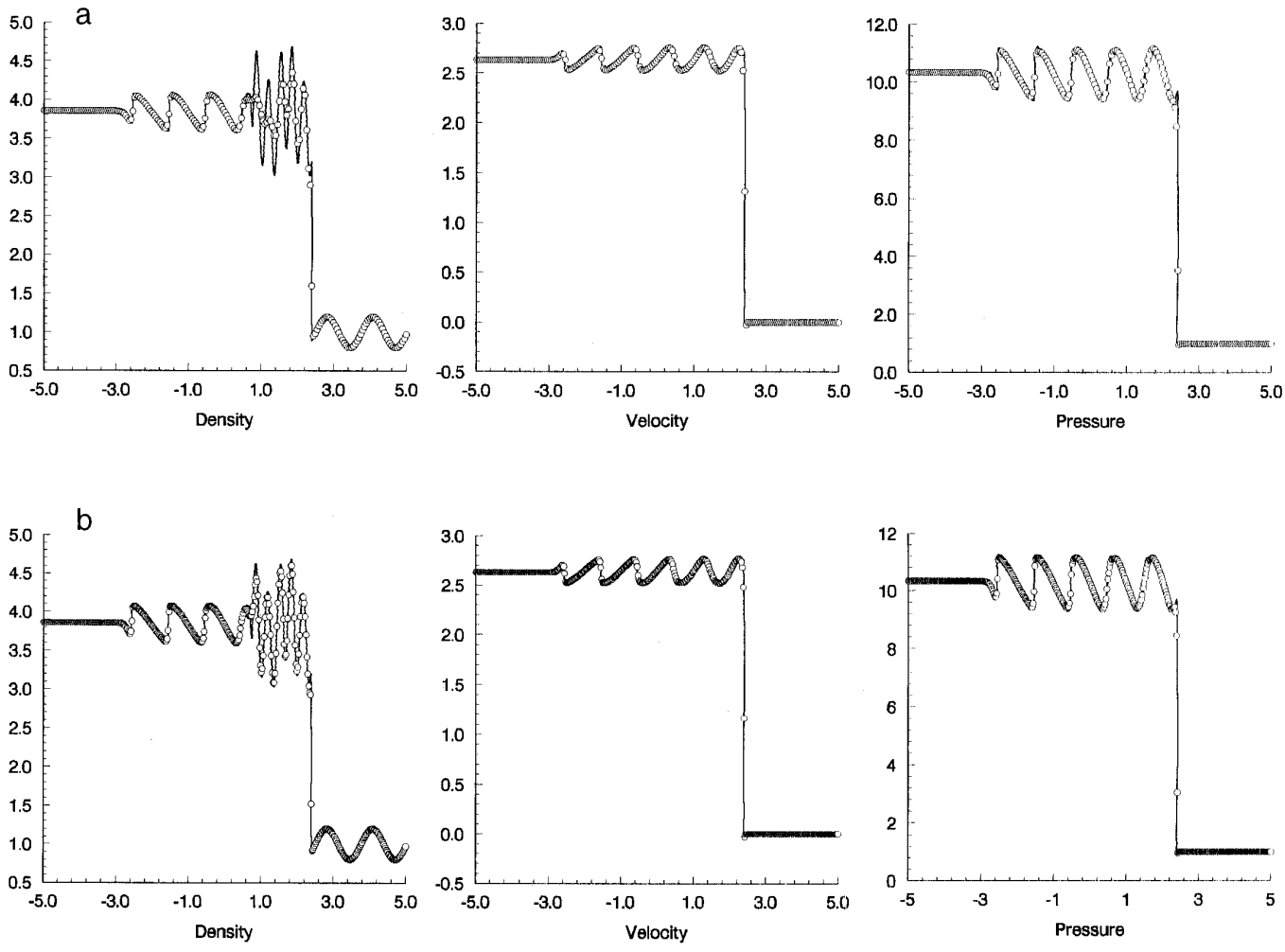

FIG. 9. Numerical solutions of shock/turbulence interactions: (a) 200 grid points; (b) 400 grid points.

CFL = 0.4. The characteristic interpolations are used in the calculations.

In Figs. 8a–h we show the solution with 400 grid points at $t = 0.01$, 0.016, 0.026, 0.028, 0.030, 0.032, 0.034, and 0.038, respectively. The continuous line in Fig. 8 is the solution with 1000 grid points. Comparing this solution to the "exact" solution of Woodward and Collella in [12], we see that it shows all the important features of various interactions and thus can be considered a "converged" solution. In the calculation we found the pressure at some grid points cannot preserve positive solution, and lower order interpolation was used at these points.

EXAMPLE 5. To see the performance of our schemes for the problems that have some structure, we apply it to Euler equations with the initial conditions:

$$(\rho, u, p) = \begin{cases} (3.857143, 2.629369, 10.33333), & x < 4, \\ (1 + 0.2 \sin 5x, 0, 1), & x \geq 4. \end{cases} \quad (62)$$

This is a model problem for "shock/turbulence" interaction. See [13] for a linearized analysis of this problem, and [8, 14] for numerical results. We apply our third-order scheme to this problem with $\alpha_1 = \alpha_2 = 0.5$, $\beta = 1.0$, and CFL = 0.4. The characteristic interpolations are also used in the calculation. The results for 200 and 400 grid points are shown in Fig. 9. The solid lines are numerical solutions with 1600 grid points. It can be regarded as the exact solution.

6. CONCLUDING REMARKS

A new methodology has been developed to construct compact high-order accurate nonlinear schemes for capturing discontinuities. These schemes work well both for smooth solutions and for capturing discontinuities in our numerical calculations of scalar conservation laws. We also discussed the extensions to Euler equations. The numerical solutions of the one-dimensional shock tube problem, blast

waves, and "shock/turbulence" interactions are presented. From these results, we see that the schemes give clear structures of various waves and wave interactions. In the calculations it was found that a slight undershoot of solutions near shock waves appeared at some time steps which may be caused by high-order truncation errors of the interpolations. Moreover, in the present paper the compact adaptive interpolations are constrained to tridiagonal matrix inversion. Hence only third- and fourth-order schemes have been constructed. Higher-order schemes, as well as the applications to multidimensional problems, are under investigation.

REFERENCES

1. S. K. Lele, *J. Comput. Phys.* **103,** 16 (1992).
2. D. X. Fu, Y. W. Ma, and H. Liu, in *Proc. 5th Int. Symp. on CFD, 1993, Sendai, Japan.*
3. X. G. Deng, H. Maekawa, and C. Shen, AIAA Paper 96-1972; in *27th AIAA Fluid Dynamics Conference, New Orleans, June 1996.*
4. A. Harten, *J. Comput. Phys.* **41,** 329 (1981).
5. B. Cockburn and C. W. Shu, *SIAM J. Numer. Anal.* **31,** No. 3, 607 (1994).
6. A. Harten, B. Engquist, S. Osher, and S. Chakravarthy, *J. Comput. Phys.* **71,** 213 (1987).
7. C. W. Shu and S. Osher, *J. Comput. Phys.* **77,** 439 (1988).
8. C. W. Shu and S. Osher, *J. Comput. Phys.* **83,** 32 (1989).
9. C. W. Shu, *J. Sci. Comput.* **5,** No. 2, 127 (1990).
10. S. Zalesak, "A Preliminary Comparison of Modern Shock-Capturing Schemes: Linear Advection," in *Advances in Computer Methods for Partial Differential Equations,* Vol. 6, edited by R. Vichnevetsky and R. Stepleman (IMACS, New Brunswick, NJ, 1987).
11. G. A. Sod, *J. Comput. Phys.* **27,** 1 (1978).
12. P. Woodward and P. Collella, *J. Comput. Phys.* **54,** 115 (1984).
13. J. F. McKenzie and K. O. Westphal, *Phys. Fluids* **11,** 2350 (1968).
14. R. Hannappel, *J. Comput. Phys.* **121,** 176 (1995).